

Noname manuscript No.
(will be inserted by the editor)

**1 Significant wind disturbances induced by giant
2 dunes.**

**3 First Author · Second Author · Third
4 Author · {...}**

5
6 Received: DD Month YEAR / Accepted: DD Month YEAR

7 Abstract
8 abstract
9 Keywords Boundary layer · Turbulent flow · Sand dunes · Fluide-structures
10 interactions

F. Author
first address
Tel.: +123-45-678910
Fax: +123-45-678910
E-mail: fauthor@example.com

S. Author
second address

T. Author
third address

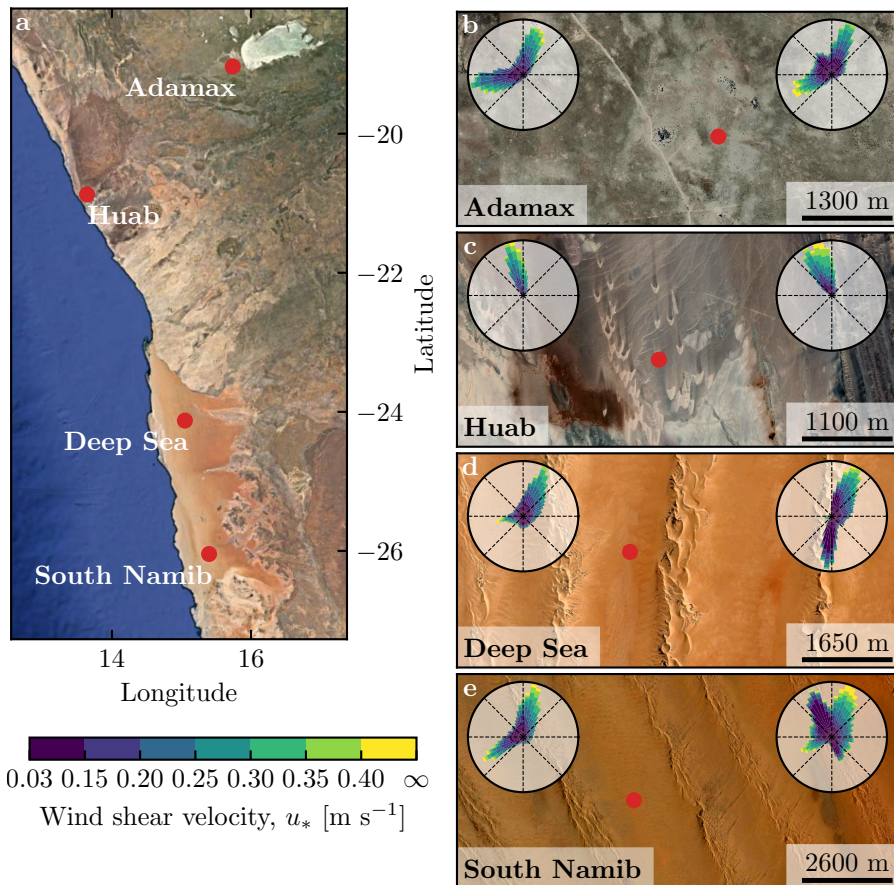


Fig. 1 Wind data used in this study **a**: Location of the studied sites. **b–e**: Satellite images of the studied sites (Google-Earth, Maxar Technologies, CNES/Airbus). In each subplot, the left and right wind roses represent the data from the ERA5Land climate reanalysis and the in situ stations, respectively. Note that the bars show the direction towards which the wind blows. The red dots show the location of the in situ stations.

11 1 Introduction

12 2 Wind regimes across the Namib Sand Sea

13 2.1 Datasets

14 Two wind datasets are used in this study. First, local winds are provided by
 15 stations situated in different environments (see Fig. 1). The wind strength and
 16 direction are measured every 10 minutes by cup anemometers and wind vanes,
 17 at heights between n and n meters depending on the station. The available
 18 period of measurements ranges from 1 to 5 discontinuous years distributed
 19 between 2012 and 2020 (see Fig. S1). We checked that at least one complete

20 seasonal cycle is available at each station. Then, regional winds are extracted
21 at the same locations and periods from the ERA5-Land dataset, which is a
22 replay at a smaller spatial resolution of ERA5, the latest climate reanalysis
23 from the ECMWF (Hersbach et al. 2020; Muñoz-Sabater et al. 2021). It
24 provides hourly estimates of the 10-m wind velocity and direction at a spatial
25 resolution of ~ 9 km ($0.1^\circ \times 0.1^\circ$).

26 For comparison, the local measurements are averaged into 1-hr bins cen-
27 tered on the temporal scale of the ERA5-Land estimates (see Fig. S2). As the
28 wind velocities of both datasets are provided at different heights, we convert
29 them into shear velocities (see SI section ??), characteristic of the whole tur-
30 bulent wind profile within the atmospheric boundary layer, which are then
31 used together with the wind direction for further analysis. The resulting wind
32 data are shown on the wind roses of Fig. 1(b–e).

33 Finally, the dune properties are computed using an autocorrelation method
34 from the 30-m Digital Elevation Models (DEMs) of the shuttle radar topog-
35 raphy mission (Farr et al. 2007). For the South Namib and Deep Sea stations,
36 we obtain respectively orientations of 85° and 125° , wavelengths of 2.6 km and
37 2.3 km and amplitudes of 45 m and 20 m (see SI for additional details).

38 2.2 Agreement between local and regional winds

39 The regional wind patterns in the Namib are strongly controlled by the see
40 breeze, resulting in strong northward components present in all regional wind
41 roses of figure 1, also deviated by the large scale topography (Lancaster 1985).
42 These daily winds are the strongest during the second-half of the year (Septembre-
43 January). In winter, an additional easterly component can be recorded during
44 the night, induced by the combination of katabatic winds forming on the moun-
45 tains, and infrequent ‘berg’ winds, which are responsible of the high wind ve-
46 locities observed (Lancaster 1984). The frequency of these easterly components
47 decreases from the inland to the coast, resulting in three bidirectional wind
48 regimes within the Namib Sand Sea and at the Adamax salt pan (Fig. 1(c, d,
49 e)) and one unidirectional wind regime on the coast at the outlet of the Huab
50 River.

51 In the case of the Adamax and Huab stations, these regional wind roses
52 qualitatively matches their respective in situ local measurements. However, for
53 the Deep Sea and South Namib stations, the local wind roses exhibit additional
54 components aligned with the giant dune orientation visible on the satellite
55 images.

56 Indeed, the analysis of the wind speed and direction time series shows that
57 the matching between the local and regional winds is verified for the stations
58 with flat environment at all times (Fig. 2(a–b)), as well as for the stations
59 within the giant dune field, but only during Septembre–January (Fig. 2(c–d)).
60 This agreement is statistically verified, as shown by the Fig. S5.

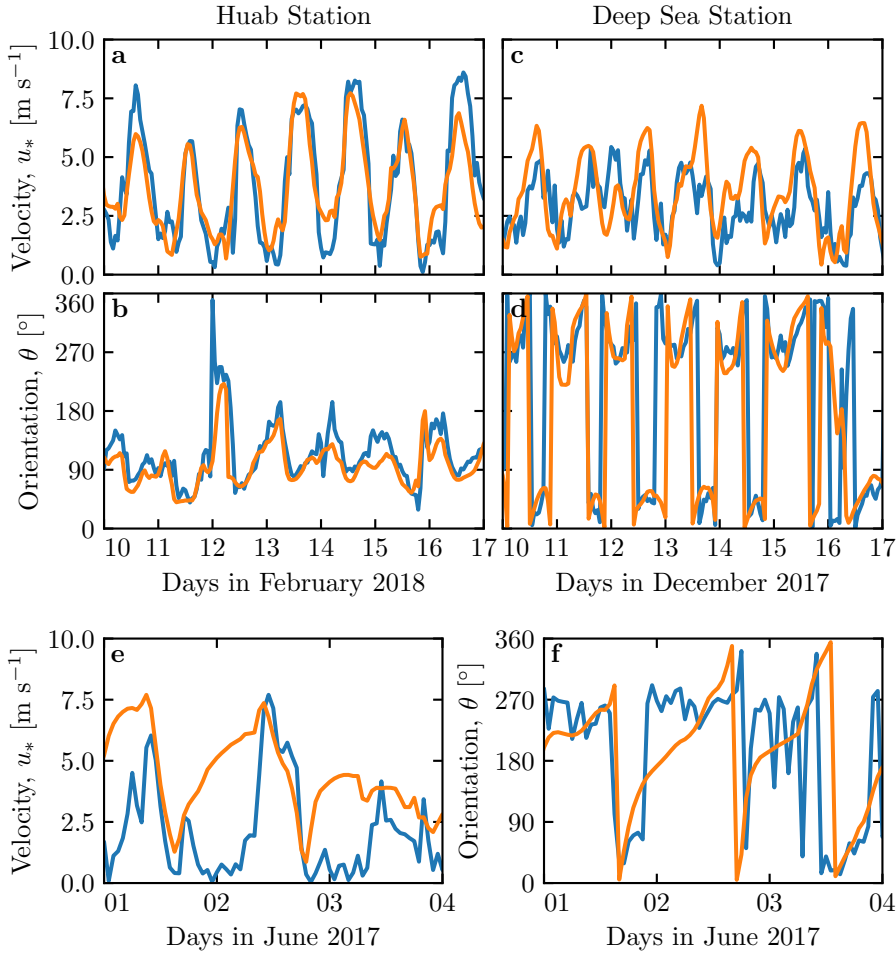


Fig. 2 Temporal comparison between the wind data coming from the Era5Land climate reanalysis (orange lines) and from the in situ measurements (blue lines). **a–b:** Huab station. **c–d:** Deep Sea station in winter. **e–f:** Deep Sea station in summer.

61 2.3 Influence of the giant dunes on local wind regimes

62 In winter, the local and regional winds match only during the morning for
 63 the stations within the giant dune field, when the southerly/southwesterly
 64 sea breeze dominates (see Fig. 2(e–f), Fig. 3 and Fig. S6). In the late after-
 65 noon and during the night, when the northwesterly ‘berg’ and katabatic winds
 66 blow, the two datasets differ. More specifically, this mismatch mainly occurs
 67 during at low wind velocities. In this case, the angular wind distribution of
 68 the local measurements exhibits two additional modes separated of $\simeq 180^\circ$,
 69 each corresponding to the giant dune alignment (purple frame in Fig. 3 and
 70 Fig. S6). This deviation at low wind velocities is statistically verified, and is

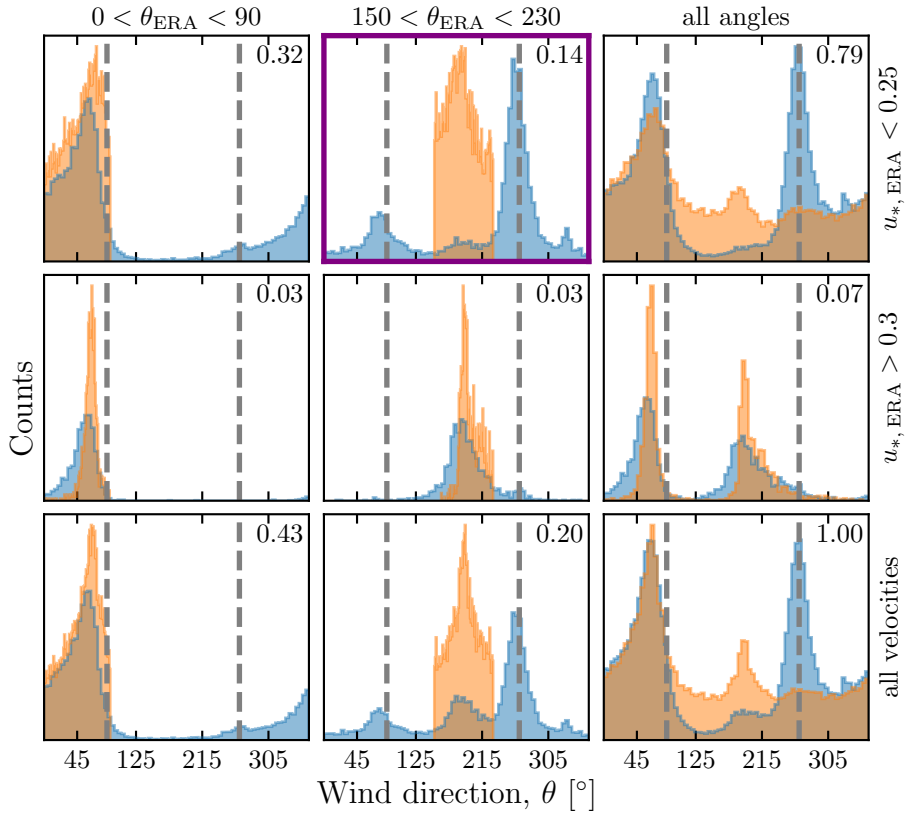


Fig. 3 Distributions of wind direction at the Deep Sea Station for the Era5Land climate reanalysis (orange) and the in situ measurements (blue). In each subplot, both distributions are plotted from the same time steps, selected with constraints on the wind direction (columns) and/or wind velocity (rows) in the Era5Land dataset. The vertical gray dashed lines indicate the dune orientation, and the top right numbers the percentage of the total number of time steps selected in each subplot. The purple frame highlights the regime (small wind velocities, nocturnal summer wind) during which the wind data from both datasets differs. A similar figure can be obtained for the Deep Sea station (see Fig. S6).

71 also associated with a global attenuation of the wind strength (Fig. S6 and
 72 Fig. S7).

73 **3 Influence of the circadian cycle of the atmospheric boundary
 74 layer**

75 Previous studies have linked meteorological flow around and over obstacles
 76 to the vertical structure of the atmosphere (Stull 1988). At the dune scale,
 77 its lower part, the turbulent atmospheric boundary layer (ABL), is directly
 78 influenced by the planetary surface (Stull 1988). When the latter is warmer
 79 than the ambient air (typically during the day), a strong convection takes

place, resulting in a logarithmic wind profile and a vertically constant potential temperature θ (which corresponds to the air density corrected from the vertical pressure variation). During the night, the surface cools faster than the ambient air, which can result in a stable layer close to the surface (typically the first 200 meters). Above, the free atmosphere (FA) is a stably stratified zone in which turbulence is negligible, and where the flow is usually considered as incompressible and inviscid. In the middle, a transitional layer, also known as entrainment zone, is characterized by a sharp increase of the potential temperature, which traps turbulence resulting from the surface friction below it. As it is much shallower than the other two layers, we consider it as capping singularity inducing a discontinuity in the potential temperature profile.

91 3.1 Relevant non-dimensional parameters and physical modeling

92 As a result, the giant dunes evolve in a turbulent flow capped by a stratified atmosphere, with a transitional layer acting as a free surface in between.
 93 When the dune are small enough, typically in the case of dune emergence
 94 or early coarsening (Fig. 4b), they do no interact with the top of the ABL
 95 (Fourriere et al. 2010). However, the giant dunes present in the Deep Sea and
 96 South Namib stations have wavelengths comparable or larger than typical
 97 ABL depths, inducing their interaction with the capping layer and the free
 98 atmosphere above (Andreotti et al. 2009). However, as sketched in Fig. 4c–d,
 99 the nature of this interaction depends on two non-dimensional number, both
 100 called Froude numbers in the literature (Vosper 2004; Sheridan and Vosper
 101 2006; Hunt et al. 2006; Jiang 2014).

102 The ability of the capping layer to deform under the presence of an underlying topography is controlled by the *surface Froude number*, typically used in
 103 the context of bedforms in rivers (Fourriere et al. 2010; Andreotti et al. 2012):

$$\mathcal{F}r_S = \frac{U}{\sqrt{\frac{\Delta\rho}{\rho} g H}}, \quad (1)$$

106 where U is the wind velocity at the top of the ABL, H its depth, ρ its average
 107 density and $\Delta\rho$ the density jump between the ABL and the FA. Likewise, the
 108 FA stratification ability to deform is controlled by the *internal Froude number*,
 109 typically used in the context of flow disturbances induced by mountains (Stull
 110 1988):

$$\mathcal{F}r_I = \frac{U}{HN}, \quad (2)$$

111 where N is the Brunt-Väisälä frequency, characteristic of a stratified fluid.
 112 When the flow inertia dominates over its weight ($\mathcal{F}r_S \gg 1$) and the weight
 113 of the stratification ($\mathcal{F}r_I \gg 1$), both the capping layer and the stratification
 114 deform and adapt to the underlying topography (Fig. 4d), resulting in an
 115 unconfined flow (?). However, an opposite force balance induces a rigid capping
 116 layer and/or stratification (Fig. 4c), resulting in confined flows. In this case,

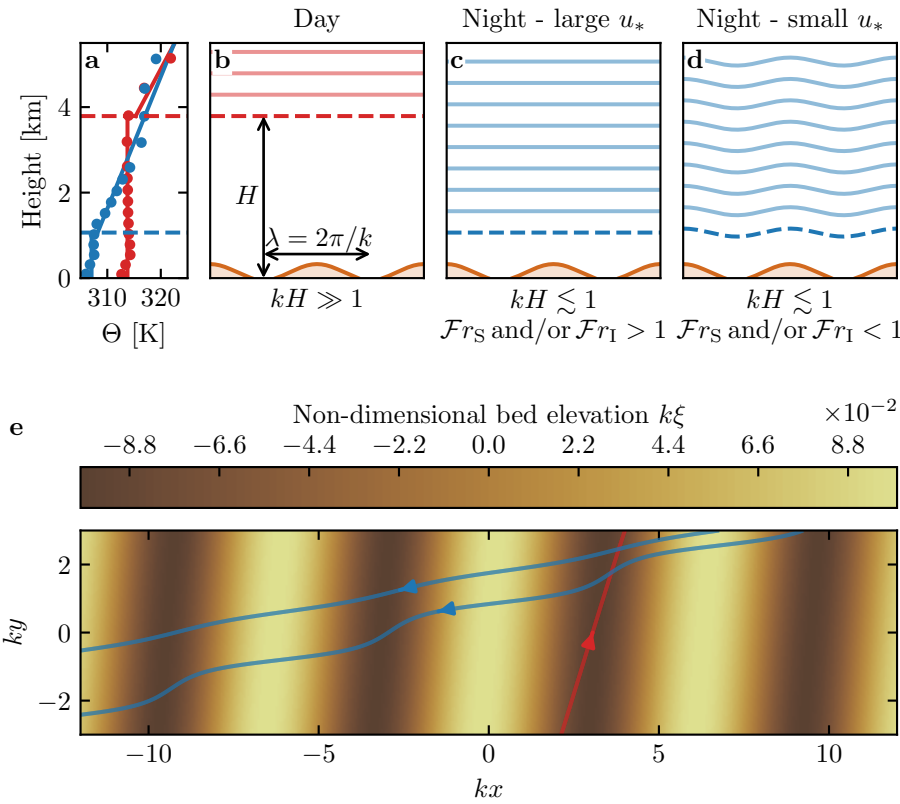


Fig. 4 **a:** Vertical profiles of the virtual potential temperature at 2 different time steps (blue - 29/11/2012 - 1100 UTC, red - 21/03/2017 - 1200 UTC) at the Deep Sea station. Dots: data from the ERA5 reanalysis. Transparent dashed lines: boundary layer height given by the ERA5 reanalysis, calculated from the bulk Richardson number (Seidel et al. 2012). Plain lines: vertical (boundary layer) and linear (free atmosphere) fits to estimate the stratification properties. **b–d:** Sketches representing the interaction between the giant dunes and the atmospheric flow for different meteorological conditions. **e:** Streamlines qualitatively representing the effect of flow confinement, in the case of the Deep Sea station. The red and straight blue lines are calculated from the unconfined case, representing the situations **b–c**. The sinuous blue line represents the confined case of **d**. For details on their derivation, see Appendix.

the confined flow has trouble going smoothly over the obstacle, and are then typically associated with large deviations and modulation of the wind velocity, as qualitatively illustrated in the case of the Deep Sea station by Fig. 4e (?).

3.2 Flow regime diagrams

In the spirit of Sheridan and Vosper (2006), we aim to compute flow regime diagrams in the space defined by the three relevant non-dimensional numbers presented above, $(kH, \mathcal{Fr}_S, \mathcal{Fr}_I)$. They are calculated from the time series of

the geopotential, temperature and specific humidity vertical profiles available in the ERA5 climate reanalysis (see SI ??). The relative velocity modulation is computed as

$$\delta_u = \frac{u_*^{\text{ERA}} - u_*^{\text{station}}}{u_*^{\text{ERA}}}, \quad (3)$$

and the flow deviation as the minimal angle between the wind orientation in the two datasets:

$$\delta_\theta = |\min([\theta_{\text{ERA}} - \theta_{\text{station}}] \bmod 360, [\theta_{\text{station}} - \theta_{\text{ERA}}] \bmod 360)|, \quad (4)$$

When these two variables are represented in the marginal spaces (kH, \mathcal{F}_{rS}) and (kH, \mathcal{F}_{rI}), different regime emerges (Fig. 5). The small wind disturbances ($\delta_\theta \rightarrow 0, \delta_u \rightarrow 0$) are located in the top-right part of the diagrams, corresponding to a regime mixing low-interactions (kH large enough, Fig. 4b) and low-confinement ($\mathcal{F}_{rS}, \mathcal{F}_{rI}$ large enough, Fig. 4c).

Lower values of kH (stronger interaction) or Froude numbers (stronger confinement) then both leads to an increase in wind disturbances, both in terms of orientation and velocity. Interestingly, the limit of no-interactions between the topography and the boundary layer structure ($kH \gg 1$), in which the properties of the capping layer and the stratification become irrelevant (Fig. 4b–4c), is never reached here, in the case of giant dunes. Below a threshold value of $kH \simeq 0.3$, wind disturbance occurs independently of the Froude numbers value. However, the latter seem to control a transition between from damped to amplified wind velocities within the interdune (Fig. 5c–5d), for which we do not have an explanation.

4 Discussion

The comparison of local and regional wind data gives a direct evidence of the giant dunes feedback on the flow. In flat areas, the matching between both datasets highlights the ability of the latest generation of climate reanalysis to predict the wind flow up to scales ~ 10 km, i.e the grid model. When smaller scale topographies are present (giant dunes in our case), locally measured wind regimes may significantly differ from the regional ones. Furthermore, we link these disturbances induced by the dunes to their interaction with the lower part of the atmospheric vertical structure, and more specifically to its circadian variability. During the day, the top of the ABL is high enough to limit the interaction of the capping layer and the FA stratification with the giant dunes, resulting in a low flow confinement, and thus small wind disturbances. During the night, the small ABL height induces a stronger flow confinement, associated with large wind deviation and acceleration or deceleration. Interestingly, we also found that this effect could be counterbalanced by the presence of large wind velocities, capable of deforming the capping layer and/or the FA stratification and thus decreasing the confinement effect.

Simple linear model such as the one of Andreotti et al. (2009) also suggests that larger wind disturbances occur under strong flow confinement such

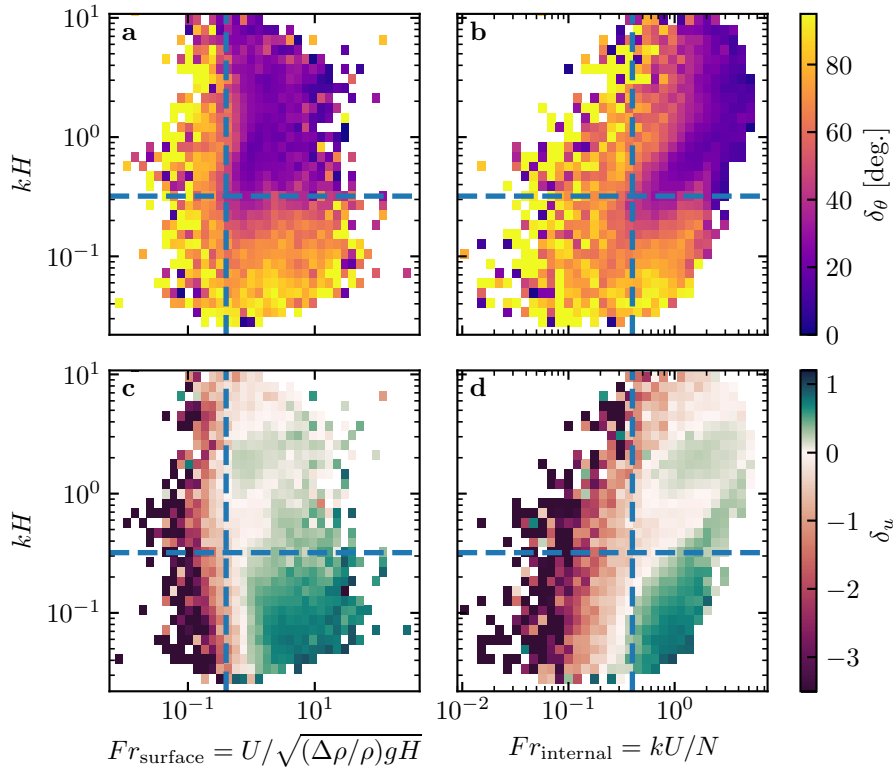


Fig. 5 Regime diagrams of the wind deviation δ_θ and relative attenuation/amplification δ_u , containing the data from both the Deep Sea and South Namib stations. Blue dashed lines empirically delimit the different regimes. The point density in each bin of the diagrams is shown in Fig. S11.

as described above. However, they are unable to reproduce the magnitude of the observed deviations, probably due to the presence of hydrodynamical non-linear effects, negligible in low confinement situations, but not otherwise (see Fig. S12 and Appendix 1). Another limit in the comparison between theoretical predictions and measured is induces by the the single-point measurements. To have reliable representations of the flow structures related to wind disturbances, additional measurements in different places on and near the same topographical obstacle are needed.

This study highlights the interaction between giant dunes and the atmospheric boundary layer, thus supporting for example the way the capping layer acts as a bounding surface limiting dune growth (Andreotti et al. 2009; Gunn et al. 2021). This interaction also have implications at smaller scales, where bedforms then develop from the disturbed wind instead of the regional one. Differences between larger and smaller scale (thus older and more recent) dune patterns are observed ubiquitously, and have sometimes in the literature been attributed to climatic changes in wind regimes (?). Here, we suggest using

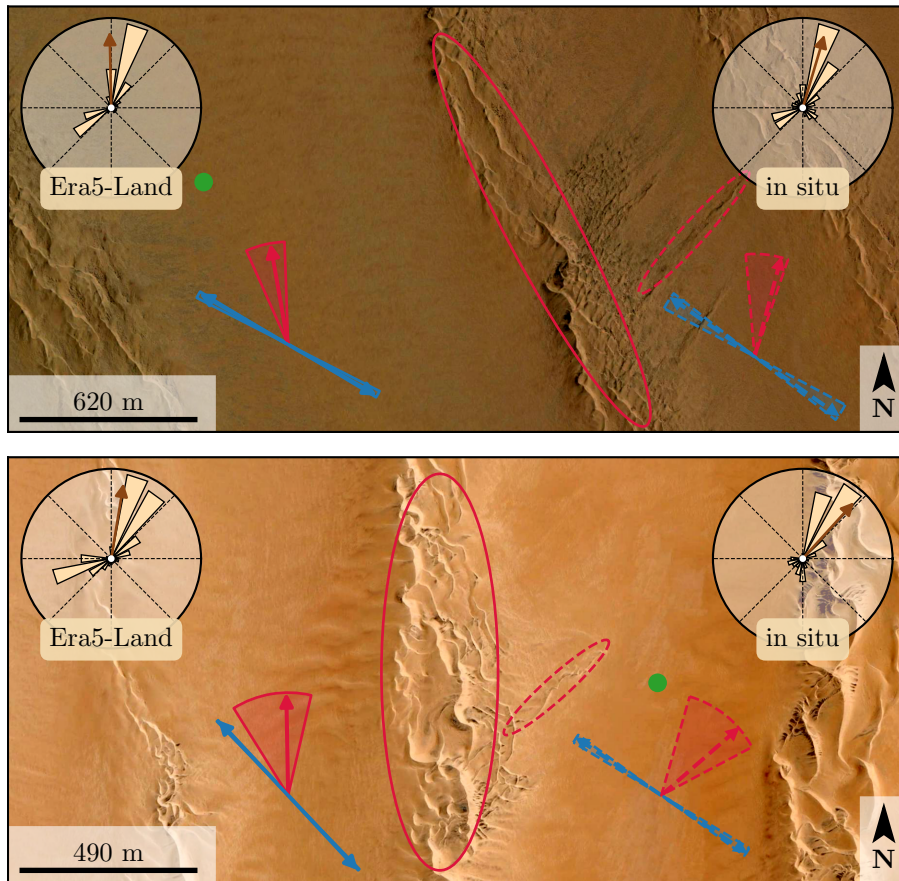


Fig. 6 Implications for smaller scale patterns in (a) the South Namib and (b) Deep Sea. The ellipses indicates the different types of elongating dunes, at large (plain) and small scale (dashed). The dune orientations are calculated using the model of ? from the sand flux angular distributions, shown here for typical sand quartz grains of $180\ \mu\text{m}$. The double blue and single red arrows correspond to the two possible dune growth mechanisms, bed instability and elongation, respectively. Likewise, plain arrows are calculated from the ERA5-Land datasets, and dashed arrows from the in situ measurements. Wedges show the uncertainty on the orientation calculation, and the arrows correspond to typical parameters found in the literature, i.e. a grain diameter of $180\ \mu\text{m}$ and a flux-up ratio of 1.6. The green dots indicate the position of the measurement stations. See Appendix 2 for details.

179 this feedback mechanism that current winds can explain dune patterns at all
 180 scales, such as the linear dunes ($\sim 50\text{ m}$ -wide) elongating within the interdune
 181 between two giant linear dunes ($\sim 2\text{ km}$ -wide) in the Namib Sand Sea (see
 182 Fig. 6).

183 **Acknowledgements** These should follow the concluding section of the paper and precede
 184 the References and any appendices, if they are present. The acknowledgements section does
 185 not require a section number.

186 Appendix 1: ABL turbulent wind model

187 Following the work of Fourriere et al. (2010) and Andreotti et al. (2012),
 188 we briefly expose in this section the linear response of a turbulent flow to a
 189 small aspect ratio perturbation of the topography ξ . As this topography can
 190 be decomposed into several sinusoidal modes, we focus on the response to a
 191 sinusoidal topography as:

$$\xi = \xi_0 \cos [k (\cos(\alpha)x + \sin(\alpha)y)], \quad (5)$$

192 which is also a good approximation to the giant dunes observed in the Deep
 193 Sea and South Namib Station (see Fig 1 and Fig S4). Here, x and y are
 194 the streamwise and spanwise coordinates, $k = 2\pi/\lambda$ the wavenumber of the
 195 sinusoidal perturbation, and α its crest orientation, calculated with respect to
 196 the y -direction.

197 In terms of basal shear stress $\tau = \rho u_*^2$, the flow response can then generally
 198 be written in as:

$$\tau_x = \tau_0 \left(1 + k\xi_0 \sqrt{\mathcal{A}_x^2 + \mathcal{B}_x^2} \cos [k (\cos(\alpha)x + \sin(\alpha)y) + \phi_x] \right), \quad (6)$$

$$\tau_y = \tau_0 k \xi_0 \sqrt{\mathcal{A}_y^2 + \mathcal{B}_y^2} \cos [k (\cos(\alpha)x + \sin(\alpha)y) + \phi_y], \quad (7)$$

199 where τ_0 is the basal shear stress on a flat bed, and $\phi_{x,y} = \tan^{-1}(\mathcal{B}_{x,y}/\mathcal{A}_{x,y})$.
 200 The in-phase and in-quadrature hydrodynamical coefficients $\mathcal{A}_{x,y}$ and $\mathcal{B}_{x,y}$
 201 are functions of the flow conditions, i.e the bottom roughness, the free surface
 202 or the incident flow direction (Fourriere et al. 2010; Andreotti et al. 2009, 2012;
 203 ?).

204 Andreotti et al. (2012) have shown that the impact of the incident wind
 205 direction can be well approximated by the following expressions:

$$\mathcal{A}_x = \mathcal{A}_0 \cos^2 \alpha, \quad (8)$$

$$\mathcal{B}_x = \mathcal{B}_0 \cos^2 \alpha, \quad (9)$$

$$\mathcal{A}_y = \frac{1}{2} \mathcal{A}_0 \cos \alpha \sin \alpha, \quad (10)$$

$$\mathcal{B}_y = \frac{1}{2} \mathcal{B}_0 \cos \alpha \sin \alpha, \quad (11)$$

206 where \mathcal{A}_0 and \mathcal{B}_0 are now two coefficients independent of the dune orientation
 207 α . In the case of a fully turbulent boundary layer capped by a free atmosphere
 208 capping, they now only depend on kH , kz_0 , \mathcal{Fr}_I and \mathcal{Fr}_S , as detailed by
 209 Andreotti et al. (2009). More specifically, their variation in the marginal spaces
 210 (kH, \mathcal{Fr}_S) and (kH, \mathcal{Fr}_I) are shown in Fig. S12.

211 Typical values for the unconfined case are therefore $\mathcal{A}_0 = 3.4$ and $\mathcal{B}_0 = 1$.
 212 In our case of giant dunes with $k\xi_0 \sim 0.1$, significant wind disturbances are
 213 then expected when $\sqrt{\mathcal{A}_0^2 + \mathcal{B}_0^2} \sim 10$. However, this is also the limit of the
 214 linear regime where this theoretical model is applicable, as hydrodynamical
 215 non-linearities become significant when $k\xi_0 \sqrt{\mathcal{A}_0^2 + \mathcal{B}_0^2} \sim 1$.

216 Appendix 2: Sediment transport and dune morphodynamics

217 Here, we briefly detail the sediment transport and dune morphodynamics theoretical framework leading to the prediction of sand fluxes and dune orientations from wind data.

220 The sediment fluxes can been directly linked to the wind basal shear stress at each time steps t from transport laws, whose exact forms depends on the sediment transport mechanisms taken into account. In this work, we following 221 the recent work of Pähzt and Durán (2020), where the sediment flux q_{sat} on a 222 flat bed made of loose sand can be expressed as:

$$\frac{q_{\text{sat},t}}{Q} = \frac{2\sqrt{\Theta_{\text{th}}}}{\kappa\mu} (\Theta_t - \Theta_{\text{th}}) \left(1 + \frac{C_M}{\mu} [\Theta_t - \Theta_{\text{th}}] \right), \quad (12)$$

225 where $\kappa = 0.4$ is the von Kármán constant, $C_M = 1.7$ a constant, $Q = d\sqrt{(\rho_s - \rho)gd/\rho}$ is a characteristic flux, with $\rho_s = 2.6 \text{ g cm}^{-3}$ and $d = 180 \mu\text{m}$ 226 the grain density and diameter, and g the gravitational acceleration. The friction coefficient μ is taken to be the avalanche slope of the granular material, 227 i.e. ~ 0.6 . Finally, the Shields number is defined as $\Theta = \rho u_{*,t}^2 / (\rho_s - \rho)gd$, and 228 its threshold value for incipient sediment transport as been calibrated using 229 laboratory experiments to $\Theta_{\text{th}} = 0.0035$.

230 The dune orientations are then predicted from the dimensional model of 231 Courrech du Pont et al. (2014). The orientation α corresponding the bed instability 232 is then the one that maximizes the following growth rate:

$$\sigma \propto \frac{1}{HWT} \int_t q_{\text{crest},t} |\sin(\theta_t - \alpha)|, \quad (13)$$

235 where H and W are dimensional constants representing the dune height and 236 width, respectively. The flux at the crest is expressed as:

$$q_{\text{crest},t} = q_{\text{sat},t} [1 + \gamma |\sin(\theta_t - \alpha)|], \quad (14)$$

237 where the flux-up ratio γ has been calibrated to 1.6 using field studies, under- 238 water laboratory experiments and numerical simulations. Similarly, the dune 239 orientation corresponding to the elongation mechanism is the one that verifies:

$$\tan(\alpha) = \frac{\langle q_{\text{crest},t}(\alpha) \mathbf{e}_{\theta_t} \rangle \cdot \mathbf{e}_{WE}}{\langle q_{\text{crest},t}(\alpha) \mathbf{e}_{\theta_t} \rangle \cdot \mathbf{e}_{SN}}, \quad (15)$$

240 where $\langle \cdot \rangle$ denotes a vectorial time average. The unitary vectors \mathbf{e}_{WE} , \mathbf{e}_{SN} and 241 \mathbf{e}_{θ_t} are in the West–East, South–North and wind direction, respectively.

242 The computed dune orientations, blue and red arrows in figure 6, are how- 243 ever depending on a large number of parameters, for which we took typical 244 values for eolian desert on Earth. We therefore run a sensibility test by calculat- 245 ing the dune orientations for grain diameters ranging from $100 \mu\text{m}$ to $400 \mu\text{m}$ 246 and the speed-up ratio from 0.1 to 10 (wedges on figure 6). We also checked 247 the sensibility the transport low by repeating the process with the quadratic 248 transport also used for comparison in Pähzt and Durán (2020), which led to 249 no more than $n\%$ of variation with respect to (12).

250 **References**

- 251 Andreotti B, Fourriere A, Ould-Kaddour F, Murray B, Claudin P (2009) Gi-
252 ant aeolian dune size determined by the average depth of the atmospheric
253 boundary layer. *Nature* 457(7233):1120–1123
- 254 Andreotti B, Claudin P, Devauchelle O, Durán O, Fourrière A (2012) Bedforms
255 in a turbulent stream: ripples, chevrons and antidunes. *Journal of Fluid
256 Mechanics* 690:94–128
- 257 Courrech du Pont S, Narteau C, Gao X (2014) Two modes for dune orientation.
258 *Geology* 42(9):743–746
- 259 Farr TG, Rosen PA, Caro E, Crippen R, Duren R, Hensley S, Kobrick M,
260 Paller M, Rodriguez E, Roth L, et al. (2007) The shuttle radar topography
261 mission. *Reviews of geophysics* 45(2)
- 262 Fourriere A, Claudin P, Andreotti B (2010) Bedforms in a turbulent stream:
263 formation of ripples by primary linear instability and of dunes by nonlinear
264 pattern coarsening. *Journal of Fluid Mechanics* 649:287–328
- 265 Gunn A, Wanker M, Lancaster N, Edmonds DA, Ewing RC, Jerolmack DJ
266 (2021) Circadian rhythm of dune-field activity. *Geophysical Research Letters*
267 48(5):e2020GL090,924
- 268 Hersbach H, Bell B, Berrisford P, Hirahara S, Horányi A, Muñoz-Sabater
269 J, Nicolas J, Peubey C, Radu R, Schepers D, et al. (2020) The era5
270 global reanalysis. *Quarterly Journal of the Royal Meteorological Society*
271 146(730):1999–2049
- 272 Hunt JCR, Vilenski GG, Johnson ER (2006) Stratified separated flow around
273 a mountain with an inversion layer below the mountain top. *Journal of Fluid
274 Mechanics* 556:105–119
- 275 Jiang Q (2014) Applicability of reduced-gravity shallow-water theory to
276 atmospheric flow over topography. *Journal of the Atmospheric Sciences*
277 71(4):1460–1479
- 278 Lancaster LNSM J (1984) Climate of the central namib desert. *Madoqua*
279 1984(1):5–61
- 280 Lancaster N (1985) Winds and sand movements in the namib sand sea. *Earth
281 Surface Processes and Landforms* 10(6):607–619
- 282 Muñoz-Sabater J, Dutra E, Agustí-Panareda A, Albergel C, Arduini G, Bal-
283 samo G, Boussetta S, Choulga M, Harrigan S, Hersbach H, et al. (2021)
284 Era5-land: A state-of-the-art global reanalysis dataset for land applications.
285 *Earth System Science Data Discussions* pp 1–50
- 286 Pähzt T, Durán O (2020) Unification of aeolian and fluvial sediment transport
287 rate from granular physics. *Physical review letters* 124(16):168,001
- 288 Seidel DJ, Zhang Y, Beljaars A, Golaz JC, Jacobson AR, Medeiros B (2012)
289 Climatology of the planetary boundary layer over the continental united
290 states and europe. *Journal of Geophysical Research: Atmospheres* 117(D17)
- 291 Sheridan PF, Vosper SB (2006) A flow regime diagram for forecasting lee
292 waves, rotors and downslope winds. *Meteorological Applications* 13(2):179–
293 195

-
- 294 Stull RB (1988) An introduction to boundary layer meteorology, vol 13.
295 Springer Science & Business Media
296 Tritton D (2012) Physical fluid dynamics. Springer Science & Business Media
297 Vosper SB (2004) Inversion effects on mountain lee waves. *Quarterly Journal*
298 of the Royal Meteorological Society: A journal of the atmospheric sciences,
299 applied meteorology and physical oceanography 130(600):1723–1748

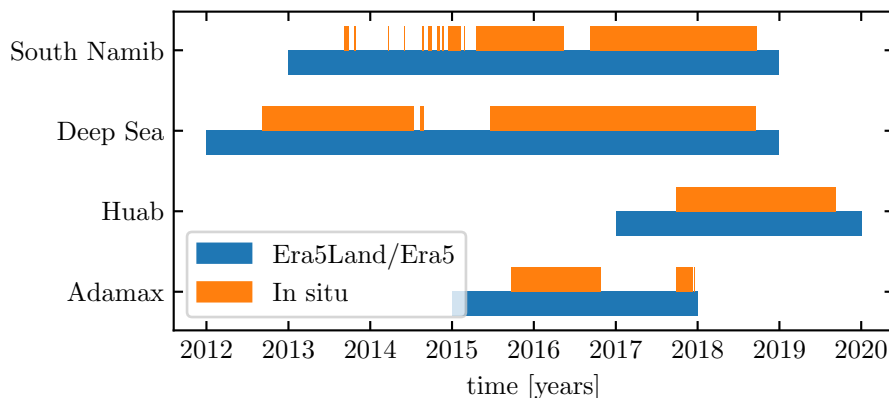


Fig. S1 Gant chart representing the usable time steps for the two data sets, for all stations.

300 **Supplementary Material for *Boundary-Layer Meteorology* Sample
301 Paper: Instructions for Authors**

302 **First Author* · Second Author · Third Author**

303
304 *Affiliation and email address for the corresponding author only (note that
305 the corresponding author does not need to be the first author).

306 **1. Calibration of the hydrodynamical roughness**

307 For each station, the hydrodynamic roughness is calibrated by finding the
308 one that minimizes the relative difference δ between the wind vectors of both
309 datasets:

$$\delta = \frac{\sqrt{\langle \| \mathbf{u}_{*,\text{era}} - \mathbf{u}_{*,\text{station}} \|^2 \rangle_t}}{\sqrt{\langle \| \mathbf{u}_{*,\text{era}} \|^2 \rangle_t \langle \| \mathbf{u}_{*,\text{station}} \|^2 \rangle_t}} \quad (16)$$

310 This δ -parameter is computed for hydrodynamic roughness values ranging
311 from 10^{-5} m to 10^{-2} m for the different stations. As shown by figure S3,
312 the minimum of δ in the space ($z_0, \text{Era}, z_0, \text{in situ}$) forms a line. We thus take
313 the roughness of the Era5Land dataset as the typical value when sediment
314 transport occurs, 10^{-3} m, corresponding to the thickness of the transport
315 layer (?). It leads for the Adamax, Deep Sea, Huab and South Namib stations
316 values of 2.7 mm, 0.76 mm, 0.12 mm and 0.48 mm, respectively.

317 The choice of the hydrodynamic roughness values only impacts the cal-
318 culated shear velocities, but note the wind directions. As such, most of our
319 conclusions are then independent of such a choice, and only the magnitude of
320 the wind velocity attenuation in confined situation might be affected.

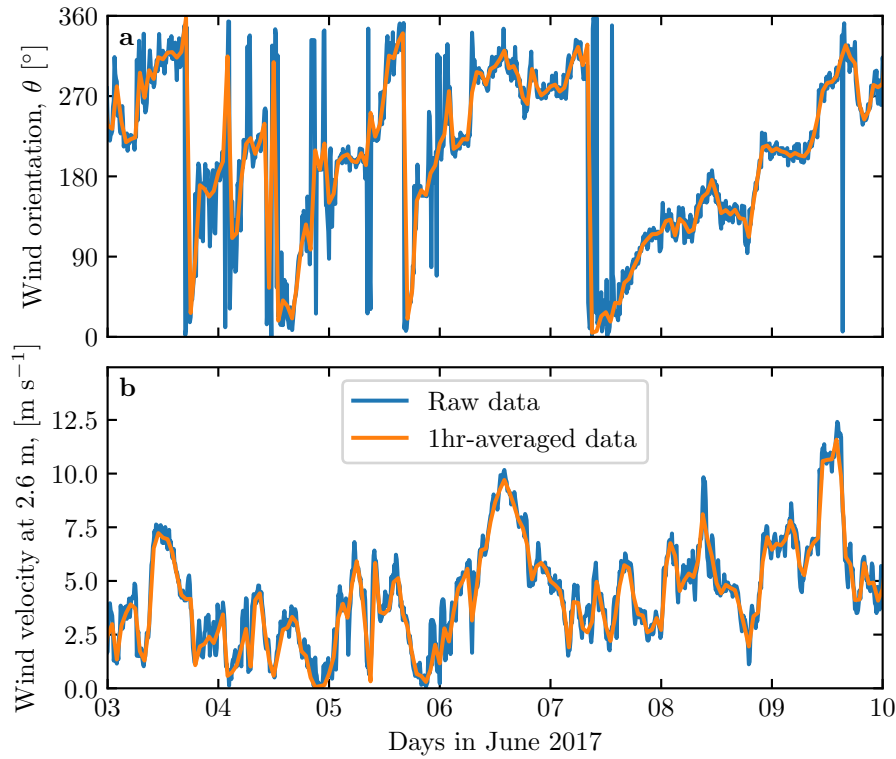


Fig. S2 Comparison between raw in situ wind measurements, and centered averaged data over one hour for the South Namib station. **a:** wind direction. **b:** wind velocity at the measurement height, 2.6 m.

321 2. Extraction of the ABL properties

322 In order to estimate the relevant non-dimensional numbers, one need to es-
 323 timate in addition to the wind and dune properties some parameters of the
 324 ABL. The Era5 dataset provides a direct bulk estimate of the ABL depth H
 325 from a bulk Richardson number calculation, as well as vertical profiles of the
 326 geopotential ϕ , temperature T and specific humidity e_w at given pressure lev-
 327 els P . From these quantities, the virtual potential temperature, which takes
 328 into account the vertical pressure and humidity changes, can be calculated as:

$$T_{vp} = T (1 + [R_M - 1] e_w) \left(\frac{P_0}{P} \right)^{P_c(1-0.24e_w)}, \quad (17)$$

329 where $P_0 = 10^5$ Pa is the standard pressure, $P_c = 0.2854$ the Poisson coefficient
 330 for dry air and $R_M = 1.61$ is the ratio between the molecular masses of dry
 331 air and water. The vertical coordinates are calculated as:

$$z = \frac{\phi R_t}{g R_t - \phi}, \quad (18)$$

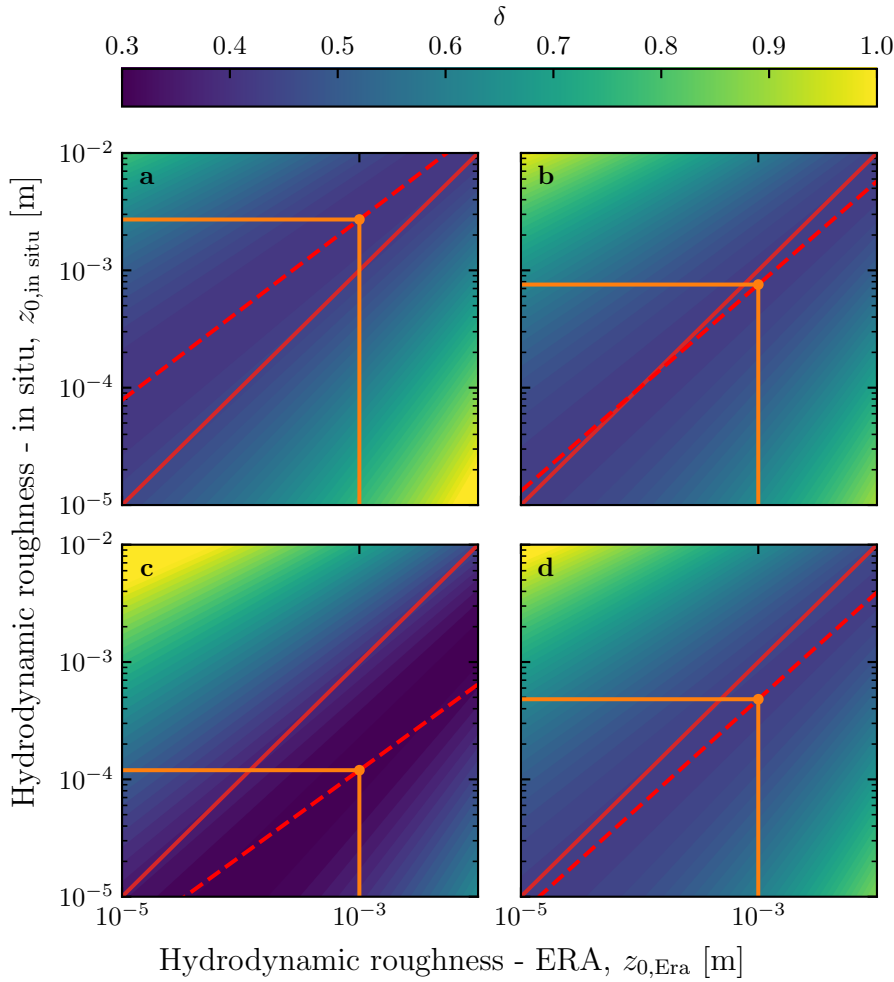


Fig. S3 Calibration of the hydrodynamic roughnesses. The metric δ defined in (16) is represented in colorscale as a function of the hydrodynamic roughnesses chosen for the Era5-Land and in situ datasets, for the Adamax (**a**), Deep Sea (**b**), Huab (**c**) and South Namib (**d**) Stations. The red dashed and plain lines shows the minima of δ and the identity line. The orange lines and dots highlights the chosen the hydrodynamic roughnesses for the in situ datasets by imposing $z_{0,\text{ERA}} = 1 \text{ mm}$, leading for each station to 2.7 mm, 0.76 mm, 0.12 mm and 0.48 mm, respectively.

332 where $R_t = 6356766 \text{ m}$ is the average Earth radius, and $g = 9.81 \text{ m s}^{-2}$ the
333 gravitational acceleration.

334 Example of obtained vertical profiles of the virtual potential temperature
335 are shown in Fig. S9. On each of them, an average is computed below the ABL
336 depth given by the Era5 dataset, and a linear function is fitted above.

337 Under the Boussinesq approximation, the temperature variations are as-
338 sumed to induce most of those of the density, leading to $\Delta\rho/\rho \simeq \Delta T_{\text{vp}}/T_{\text{vp}}$.

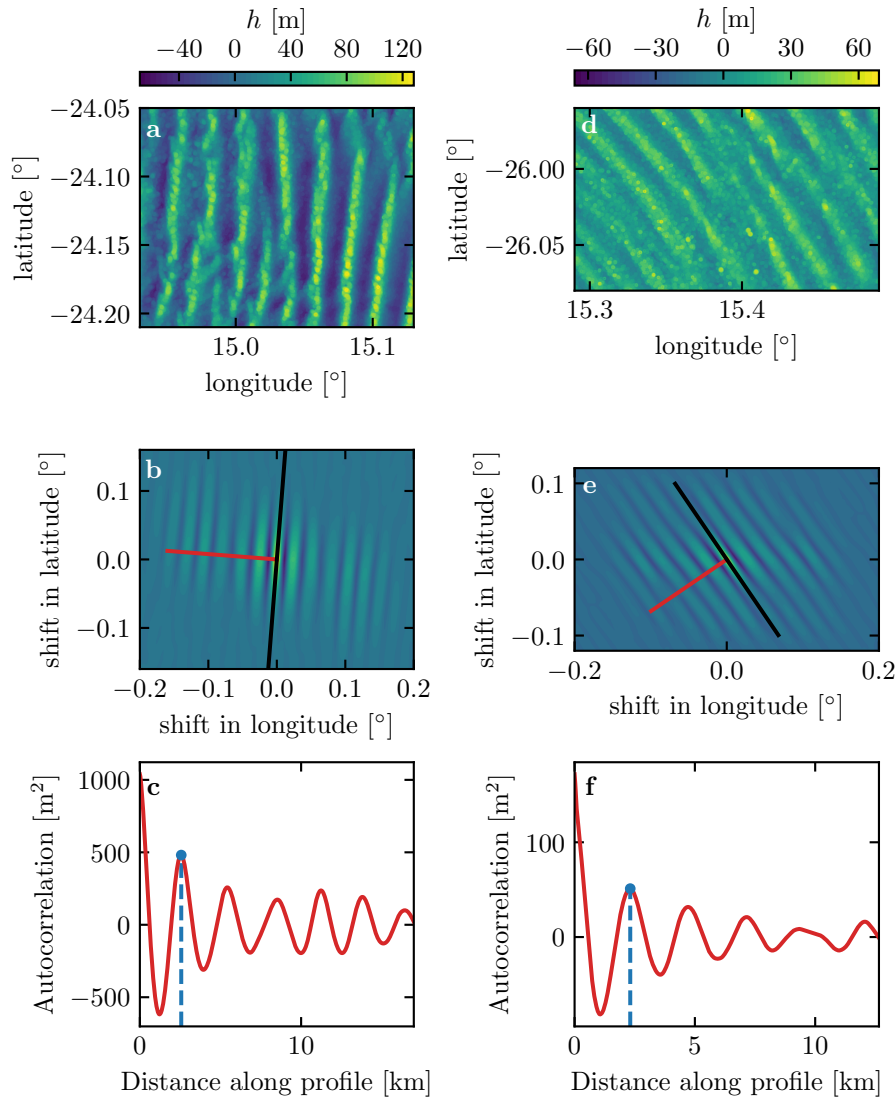


Fig. S4 Analysis of the DEMs of the Deep Sea (left column – **a**, **b**, **c**) and South Namib (right column – **d**, **e**, **f**) stations. **a–c**: Detrended topography (a second order polynomial is first fitted and then removed). **b–d**: autocorrelation matrix shown in colorscale. The black line shows the detected orientation, and the red line the profile along which the wavelength is calculated, shown in **e–f**. The blue lines and dots show the first peak of the autocorrelation profile, whose horizontal position gives the characteristic wavelength of the dune pattern.

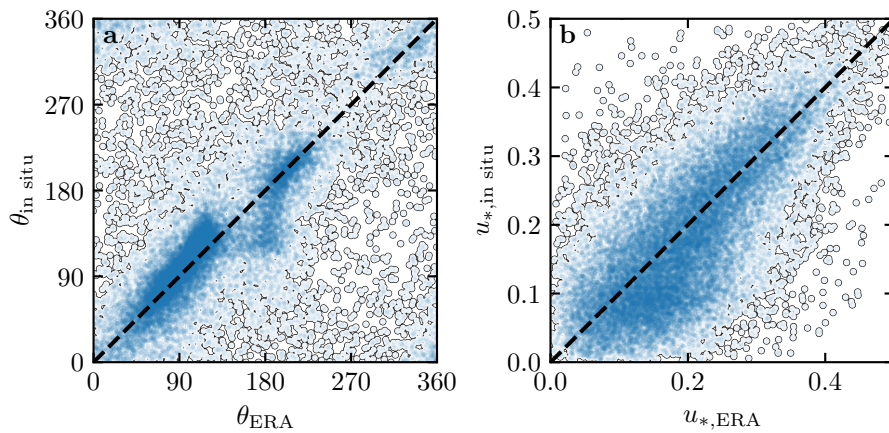


Fig. S5 Statistical agreement of the wind orientation (a) and velocity (b) between the Era5Land dataset and the in situ measurements for the Huab and Adamax stations. Note how the points are clustered around identity lines, black and dashed.

339 Here, $T_{\text{vp}}/T_{\text{vp}}$ is the relative virtual potential temperature jump at the cap-
 340 ping, directly measured on the vertical profiles.

341 Following Tritton (2012), the relative density jump at the capping layer

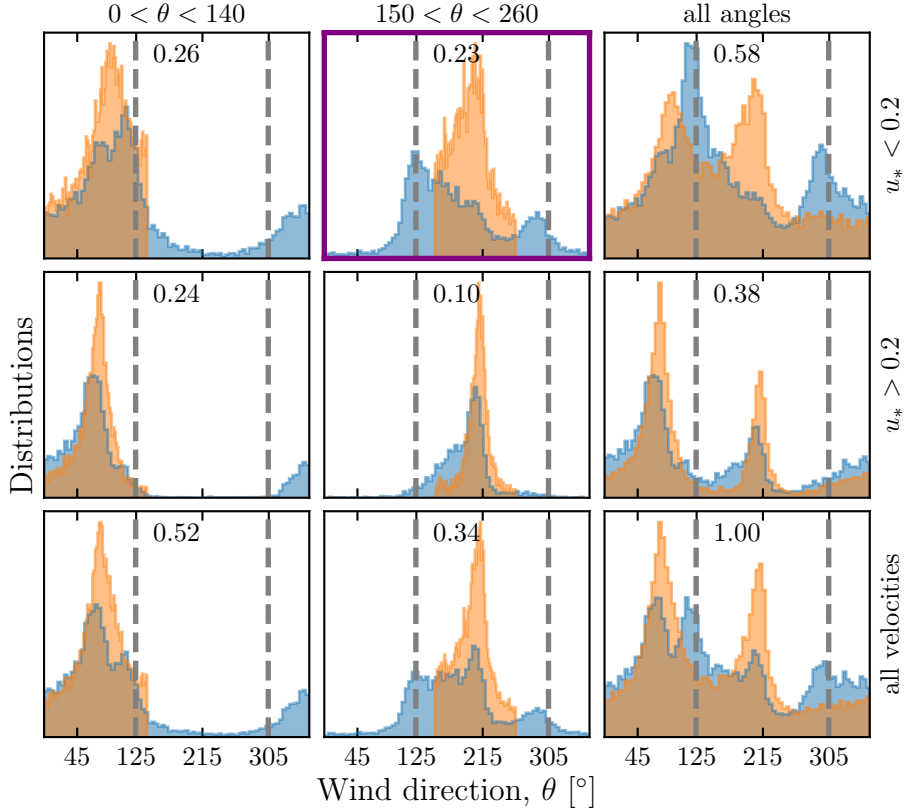


Fig. S6 Distributions of wind direction at the South Namib Station for the Era5Land climate reanalysis (orange) and the in situ measurements (blue). In each subplot, both distributions are plotted from the same time steps, selected with constraints on the wind direction (columns) and/or wind velocity (rows) in the Era5Land dataset. The grey dashed vertical lines indicate the dune orientation. The purple frame highlights the regime (small wind velocities, nocturnal summer wind) during which the wind data from both datasets differs. A similar figure can be obtained for the South Namib station (see Fig. 3).

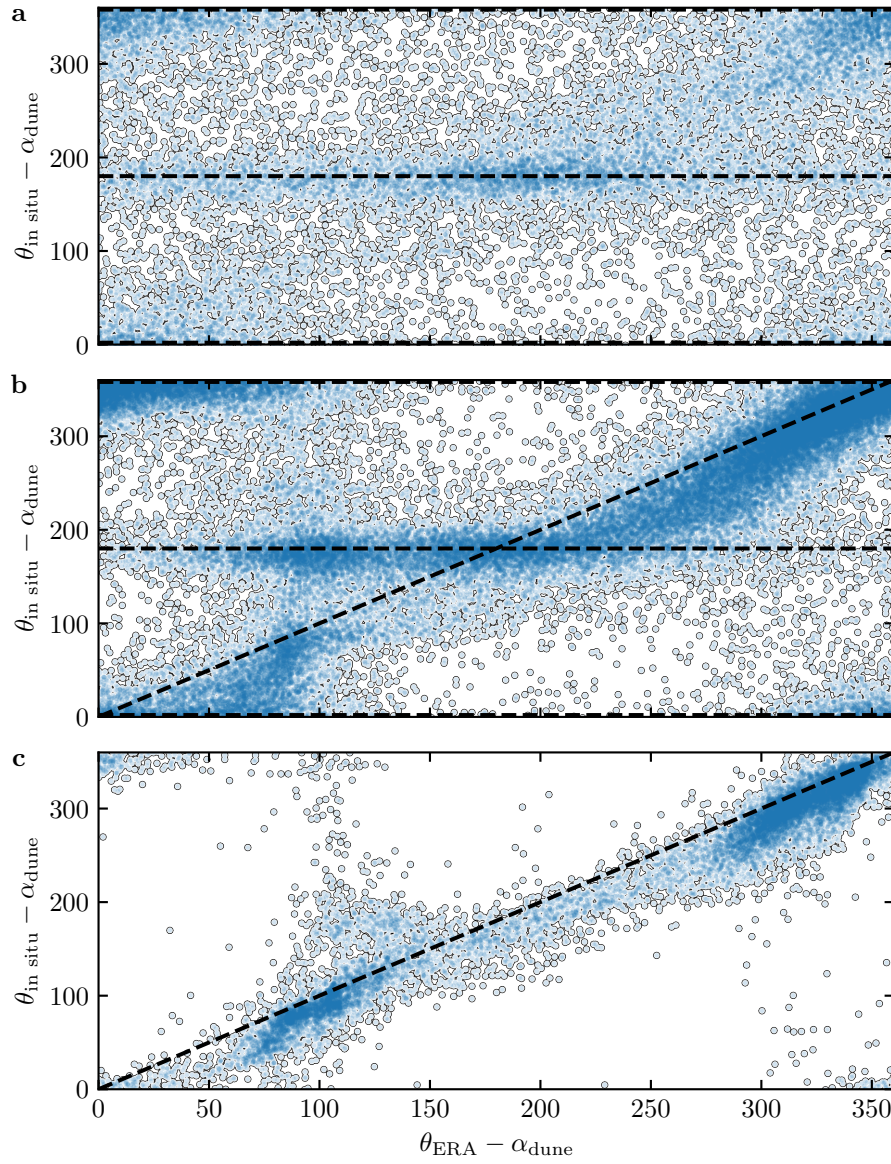


Fig. S7 Statistical comparison of the wind orientation between the Era5Land dataset and in situ measurements for the South Namib and Deep Sea stations, for different velocity ranges. **a:** $u_{*,\text{ERA}} < 0.1 \text{ m s}^{-1}$. **b:** $0.1 < u_{*,\text{ERA}} \leq 0.25 \text{ m s}^{-1}$. **c:** $u_{*,\text{ERA}} \geq 0.25 \text{ m s}^{-1}$. Note that the dune orientations measured are subtracted to the wind orientation, which allows to plot both stations on the same graph. Black dashed lines indicates in situ orientations aligned with the dune crests (here 0° , 180° and 360° – **a, b**), as well as the identity lines (**b, c**).

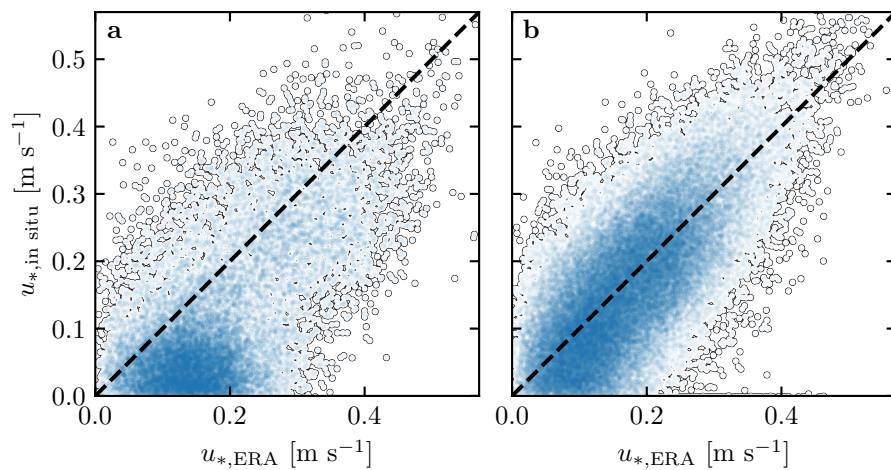


Fig. S8 Statistical comparison of the wind velocity between the Era5Land dataset and in situ measurements for the South Namib and Deep Sea stations. **a:** Nocturnal summer easterly wind. **b:** Diurnal southerly wind. Black dashed lines are identity lines. The angle ranges corresponding to diurnal and nocturnal summer winds are those taken in Fig. 3 and Fig. S6.

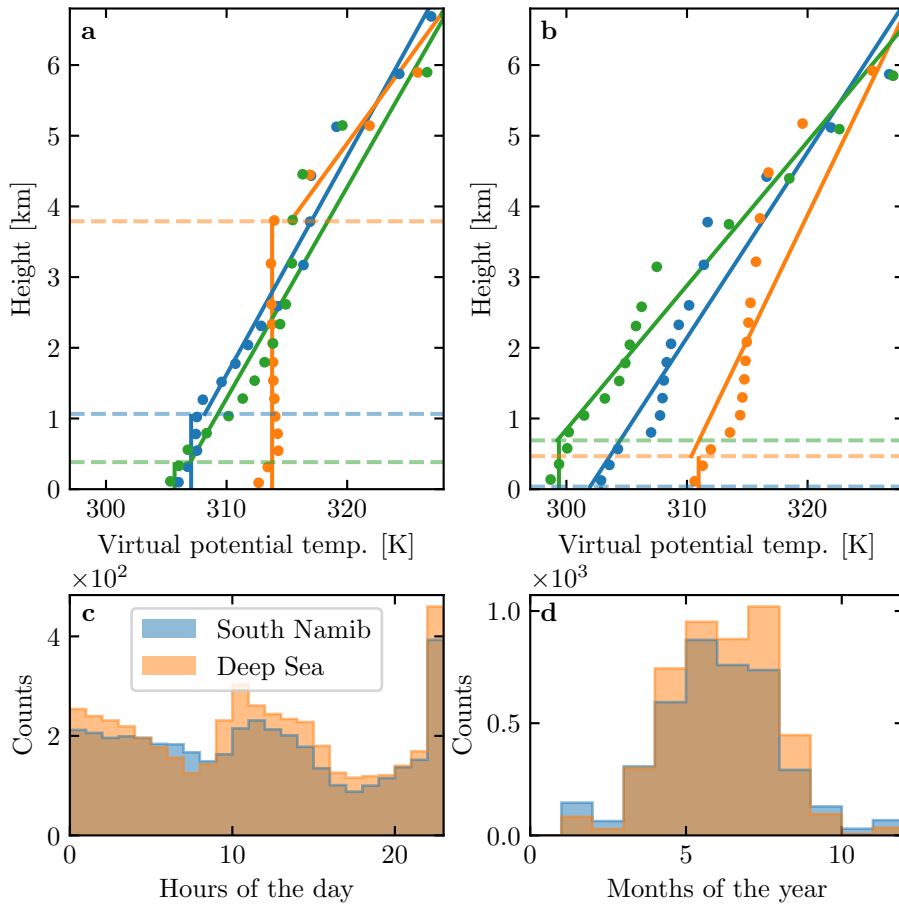


Fig. S9 **a:** Vertical profiles of the virtual potential temperature at 3 different time steps (blue - 29/11/2012 - 1100 UTC, orange - 21/03/2017 - 1200 UTC, green - 21/03/2017 - 2000 UTC) at the South Namib station. Dots: data from the ERA5 reanalysis. Transparent dashed lines: boundary layer height given by the ERA5 reanalysis, calculated from the bulk Richardson number (Seidel et al. 2012). Plain lines: vertical (boundary layer) and linear (free atmosphere) fits to estimate the quantities in Fig. S10. **b:** Examples of ill-processed vertical profiles at 3 different time steps (blue - 2/12/2013 - 2300 UTC, orange - 20/03/2017 - 0000 UTC, green - 14/07/2017 - 1400 UTC) at the South Namib station. **c:** Hourly distribution of ill-processed vertical profiles. **d:** Monthly distribution of ill-processed vertical profiles. These profiles are ill-processed because the temperature found at the boundary layer from the linear fit in the free-atm is smaller than the average one inside the boundary layer. This is an unstable situation, which does not allow to calculate the surface Froude number.

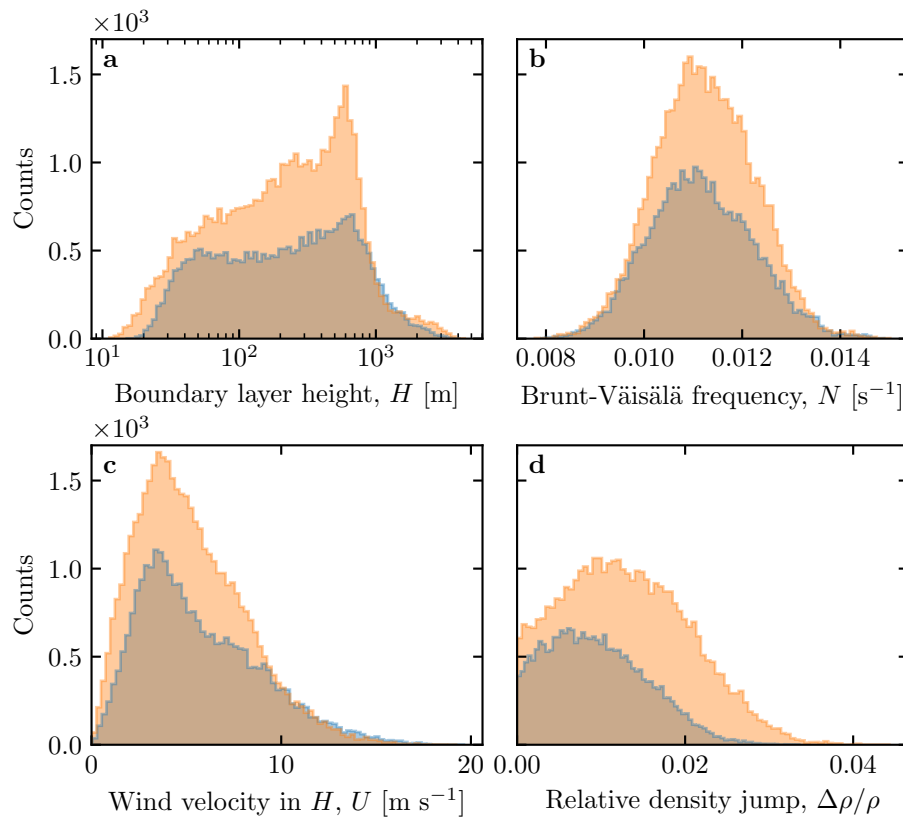


Fig. S10 Distributions of the meteorological parameters resulting from the processing of the Era5-Land data for the South Namib (blue) and the Deep Sea (orange) stations.

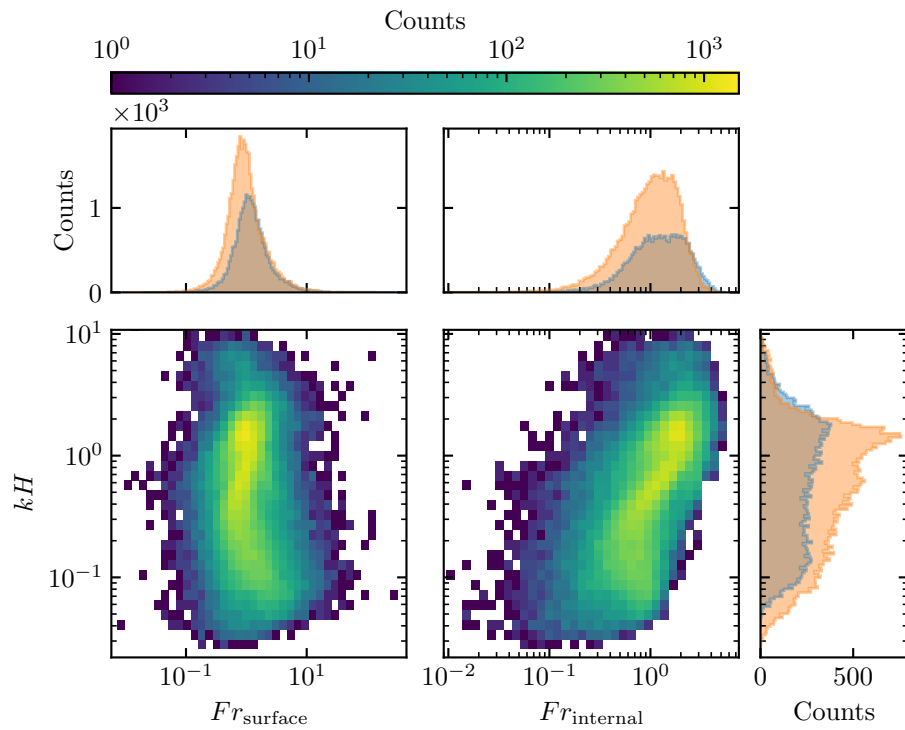


Fig. S11 Non-dimensional parameters distributions. For the marginal distributions, the orange correspond to the South Namib station, and the blue to the Deep Sea station.

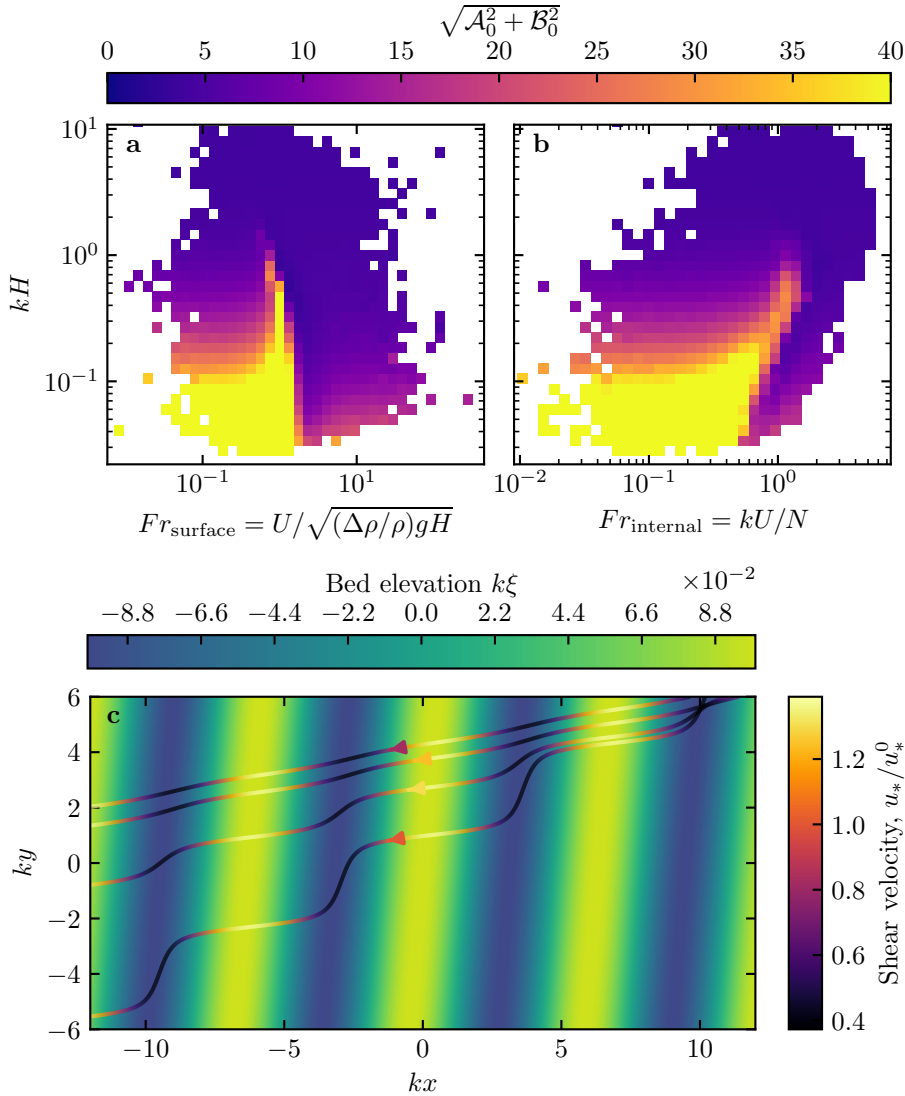


Fig. S12 Physical interpretation of the flow disturbance. (a) and (b) Magnitude of the disturbance induced by a sinusoidal topography calculated from the time series of the non-dimensional numbers presented in Figures 4 and 5 using the linear model of Andreotti et al. (2009). (c) Shear velocity streamlines represented in the case of the Deep Sea station, for increasing values of $\sqrt{\mathcal{A}_0^2 + \mathcal{B}_0^2}$. From the upper to the lower streamline, values of $(kH, Fr_{\text{surface}}, Fr_{\text{internal}}, \mathcal{A}_0, \mathcal{B}_0, \sqrt{\mathcal{A}_0^2 + \mathcal{B}_0^2})$ are $(1.9, 0.6, 1.5, 3.4, 1.0, 3.5)$, $(1.5, 0.3, 0.4, 4.8, 1.4, 5.0)$, $(0.1, 3.5, 1.0, 8.6, 0.1, 8.6)$, $(0.5, 0.05, 0.04, 9.6, 2.5, 9.9)$.